

**High-harmonic generation from strain-engineered graphene for polarization tailoring**Navdeep Rana,<sup>1</sup> M. S. Mrudul<sup>2</sup>,,<sup>2</sup> and Gopal Dixit<sup>1,3,4,\*</sup><sup>1</sup>*Department of Physics, Indian Institute of Technology Bombay, Powai, Mumbai 400076, India*<sup>2</sup>*Department of Physics and Astronomy, P.O. Box 516, Uppsala University, S-75120 Uppsala, Sweden*<sup>3</sup>*Center for Computational Sciences, University of Tsukuba, Tsukuba 305-8577, Japan*<sup>4</sup>*Max-Born Institute, Max-Born Straße 2A, 12489 Berlin, Germany*

(Received 26 February 2024; revised 23 July 2024; accepted 25 July 2024; published 5 August 2024)

Strain engineering is a versatile method to boost the carrier mobility of two-dimensional materials-based electronics and optoelectronic devices. In addition, strain is ubiquitous during device fabrication via material deposition on a substrate with a different lattice structure. Here, we show that the polarization properties of the harmonics in graphene under uniaxial strain are strongly, yet differently affected in the lower and higher orders. The polarization plane of the lower-order emitted harmonics is rotated—a manifestation of Faraday rotation due to the broken symmetry planes. In contrast, we observe elliptically polarized higher-order harmonics due to the intricate interplay of the interband and intraband electron dynamics. The implications of these findings are twofold: First, we show how the rotation of the polarization plane of the lower-order harmonics can be used as a probe to characterize the strain's nature, strength, and angle. Second, we demonstrate how strain engineering can be used to alter the polarization properties of higher-order harmonics, relevant for applications in ultrafast chiral-sensitive studies. Our research opens a promising avenue for strain-tailored polarization properties of higher-order harmonics in engineered solids.

DOI: [10.1103/PhysRevB.110.054103](https://doi.org/10.1103/PhysRevB.110.054103)**I. INTRODUCTION**

Over the past decade, strong-field-driven high-harmonic spectroscopy has transpired as a robust method to interrogate numerous properties of solids on an ultrafast timescale [1–18]. In this respect, high-harmonic generation (HHG) from the engineered solid targets is advantageous in two ways: first, by actively controlling the generation process, the properties of the emitted harmonics can be tuned, and second, as the characterization method to investigate the properties of the engineered targets [19–23]. The present work demonstrates that the engineered two-dimensional (2D) materials not only increase the cutoff of the harmonics and enhance the yield, but also offer the capability to tailor the harmonics' polarization. Necessary control over the polarization of the higher-order harmonics is quintessential to investigating a diverse range of chiral-sensitive light-matter phenomena [24–29]. In addition, we will show that the analysis of the emitted harmonics allows us to diagnose the role of modified symmetries in the engineered 2D materials.

Monolayer graphene's discovery has sparked enormous interest in synthesizing a broad family of other 2D materials [30,31]. Owing to the exceptional transport and optoelectronic properties, 2D materials have garnered tremendous attention in recent years as potential candidates for next-generation photonics and nanoelectronic devices [32–34]. There have been continuous efforts to improve device performance by tailoring the properties of the 2D materials in

a controlled manner [35,36]. Strain engineering is a highly effective technique to control a material's properties as it has three control knobs: nature (tensile or compressive), direction (along zigzag, armchair, and arbitrary), and strength of the strain [37,38]. Moreover, the presence of strain becomes unavoidable when a 2D material is grown on a substrate with different structure and lattice parameters, e.g., during the fabrication of devices such as field-effect transistors [39–41]. Over the years, strained graphene has become a playground to improve carrier mobility in graphene-based devices as well as to explore new physics [42–47]. Thus, the characterization of strain is of paramount importance for fundamental and technological applications. In recent years, the impact of strain on solids has been studied in the context of HHG [48–51]. These investigations have demonstrated that strain leads to an enhancement or a quenching of the harmonic yield.

Graphene under strain is chosen to illustrate the polarization tunability of the emitted harmonics. Moreover, analysis of the emitted harmonics allows us to characterize strain strength as small as 0.001, which corresponds to a 0.05 picometer change in bond distance between two atoms in graphene. Owing to high flexibility under external stimuli, various methods have been used to introduce strain in monolayer graphene, such as the application of mechanical pressure via scanning tunneling microscopy (STM) tips [52] or via gas inflation [53], to name but a few [54–56]. Moreover, lattice and/or thermal expansion mismatch during growth on a substrate can also introduce strain [57,58]. Polarized Raman spectroscopy is routinely employed to quantify strain in graphene by analyzing the shift in vibrational bands [59–61]. However, sensing the strain strength below 0.1% is challenging as the shift in

\*Contact author: [gdixit@phy.iitb.ac.in](mailto:gdixit@phy.iitb.ac.in)

the 2D peak position is much smaller than its peak width [62,63]. Such a limitation is not the case for high-harmonic spectroscopy.

In the following, we will show how the tensile and compressive uniaxial strains affect HHG in graphene differently. Polarization of the lower-order harmonics is observed to be rotated with respect to the driving laser. The rotation of the polarization plane of the lower-order harmonics is analogous to the optical Hall effect in strained graphene—Faraday rotation [45]. Information about the strength, direction, and nature of the uniaxial strain can be extracted by analyzing the polarization dependence of the harmonics. On the other hand, the higher-order harmonics are elliptical in nature, and their ellipticity can be tuned by the nature, strength, and direction of the strain. Experimental observations of characteristic ellipticity dependence of the higher-order harmonics in monolayer graphene [64–66] have motivated a series of theoretical work on HHG from the graphene where various aspects of the laser polarization on the HHG have been reported [67–86]. In addition, the impact of the shear strain on terahertz-driven high-order harmonics from graphene has been discussed theoretically [87].

## II. THEORETICAL METHODOLOGY

The strain tensor corresponding to a uniaxial strain on graphene is described as [88]

$$\boldsymbol{\varepsilon} = \varepsilon \begin{bmatrix} \cos^2 \theta_s - \sigma \sin^2 \theta_s & (1 + \sigma) \cos \theta_s \sin \theta_s \\ (1 + \sigma) \cos \theta_s \sin \theta_s & \sin^2 \theta_s - \sigma \cos^2 \theta_s \end{bmatrix}. \quad (1)$$

Here,  $\varepsilon$  quantifies the strain's strength, and  $\theta_s$  is the direction along which the strain is applied and measured with respect to the zigzag direction ( $X$  axis).  $\sigma = 0.165$  is the Poisson's ratio [89]. Under the uniaxial strain of strength  $\varepsilon$  along  $\theta_s$ , any undeformed vector  $\mathbf{u}$  in the real space is transformed as

$$\tilde{\mathbf{u}} = (\mathbb{1} + \boldsymbol{\varepsilon}) \cdot \mathbf{u}, \quad (2)$$

where  $\mathbb{1}$  is the  $2 \times 2$  identity matrix.

The tight-binding approach is used to describe the monolayer graphene as [90]

$$\mathcal{H}_{\mathbf{k}} = - \sum_{\langle mn \rangle} \gamma_{mn} e^{i\mathbf{k} \cdot \boldsymbol{\delta}_{mn}} \hat{a}_{m\mathbf{k}}^\dagger \hat{b}_{n\mathbf{k}} + \text{H.c.} \quad (3)$$

Here,  $\hat{a}_{m\mathbf{k}}^\dagger$  ( $\hat{a}_{m\mathbf{k}}$ ) represents the electronic creation (annihilation) operator at the  $A$  sublattice, while  $\hat{b}_{n\mathbf{k}}^\dagger$  ( $\hat{b}_{n\mathbf{k}}$ ) denotes the electronic creation (annihilation) operator at the  $B$  sublattice. The summation is performed over the nearest-neighboring atoms. An exponential function of interatomic distance describes the hopping energy as  $\gamma_{mn} = \gamma_0 e^{-(\delta_{mn}-a)/b}$  with  $\delta_{mn}$  as the separation vector between nearest-neighbor atoms,  $\gamma_0 = 2.7$  eV,  $a = 1.42$  Å as the interatomic distance, and  $b = 0.32a$  as the decay length [88]. When the uniaxial strain is applied in graphene, atomic positions and the lattice vectors are modified according to Eq. (2). Moreover, the Hamiltonian in Eq. (3) changes accordingly. The changes in the electronic structure and optical properties of the strained graphene are documented in Refs. [90,91]. As we will illustrate later, the Dirac points of graphene and high-symmetry points of the

Brillouin zone, i.e.,  $K$  and  $K'$ , do not coincide in the strained graphene.

Density-matrix-based semiconductor Bloch equations are solved numerically to simulate laser-driven electron dynamics in strained graphene [92]. The Fourier transform ( $\mathcal{FT}$ ) of the time derivative of the charge current is used to obtain the harmonic spectrum as  $|\mathcal{FT}[\partial \mathbf{J}(t)/\partial t]|^2$ , where  $\mathbf{J}(t)$  stands for the charge current generated by the driving laser. A constant phenomenological dephasing time of 10 fs is used and our findings remain qualitatively the same for dephasing times ranging from 2 to 20 fs, as shown in the Supplemental Material [93]. An 85-fs-long linearly polarized pulse with 3.2  $\mu\text{m}$  wavelength and  $10^{11}$  W/cm<sup>2</sup> peak intensity is employed. Our findings remain qualitatively the same for a laser intensity ranging from 0.8 to  $1.4 \times 10^{11}$  W/cm<sup>2</sup>, and wavelength variation from 2.0 to 4.8  $\mu\text{m}$ . The driving laser is polarized along the  $X$  direction throughout this paper, unless stated otherwise. Here, armchair and zigzag directions are aligned with the  $Y$  and  $X$  axes, respectively.

## III. RESULTS AND DISCUSSION

Let us discuss how microscopic modifications caused by the uniaxial strain impact HHG. Figure 1 present the high-harmonic spectra of graphene under the tensile and compressive strains along the  $\theta_s = 30^\circ$  direction, and the respective real-space lattice structures for different  $\theta_s$  values. The lattice structure of the unstrained graphene ( $\varepsilon = 0.0$ ) and the corresponding high-harmonic spectrum are shown as references in gray. The uniaxial strain leads to noticeable changes in the spectra. Moreover, the tensile and compressive strains distinctively affect the harmonic generation, as visible from Figs. 1(d) and 1(e), respectively. In the case of tensile strain, the lattice stretches along the strain direction and compresses in the perpendicular direction as governed by Poisson's ratio. This situation is opposite when the strain is compressive in nature [see Eqs. (1) and (2)]. The different behavior of the tensile and compressive strains is evident from the asymmetric nature of the Hamiltonian with respect to  $\varepsilon$ , described in Eq. (3). Thus, the emitted harmonics are sensitive to the nature of the applied strain.

The absence of even-order harmonics indicates that the uniaxial strain preserves the inversion symmetry in strained graphene. Interestingly, the generated harmonics are polarized parallel and perpendicular to the driving pulse's polarization. This follows the broken reflection symmetries along the  $XZ$  and  $YZ$  planes when graphene is stretched uniaxially along  $\theta_s = 30^\circ$  with respect to the zigzag direction, as evident from Fig. 1(b). The perpendicular component of higher-order harmonics is absent when strain is applied along the zigzag [Fig. 1(a)] or armchair [Fig. 1(c)] directions, as they preserve the  $XZ$  and  $YZ$  reflection planes, analogous to unstrained graphene. At this juncture, it is interesting to explore how the generation of the parallel and perpendicular components affects the polarization of the emitted harmonics. To address this crucial question, let us first focus on the low-order harmonics.

Figures 2(a) and 2(d) present projection of the time profile of the low-order harmonics corresponding to the spectra shown in Figs. 1(d) and 1(e), respectively. To obtain the time profile, the third (H3) and fifth (H5) harmonics are fitted by

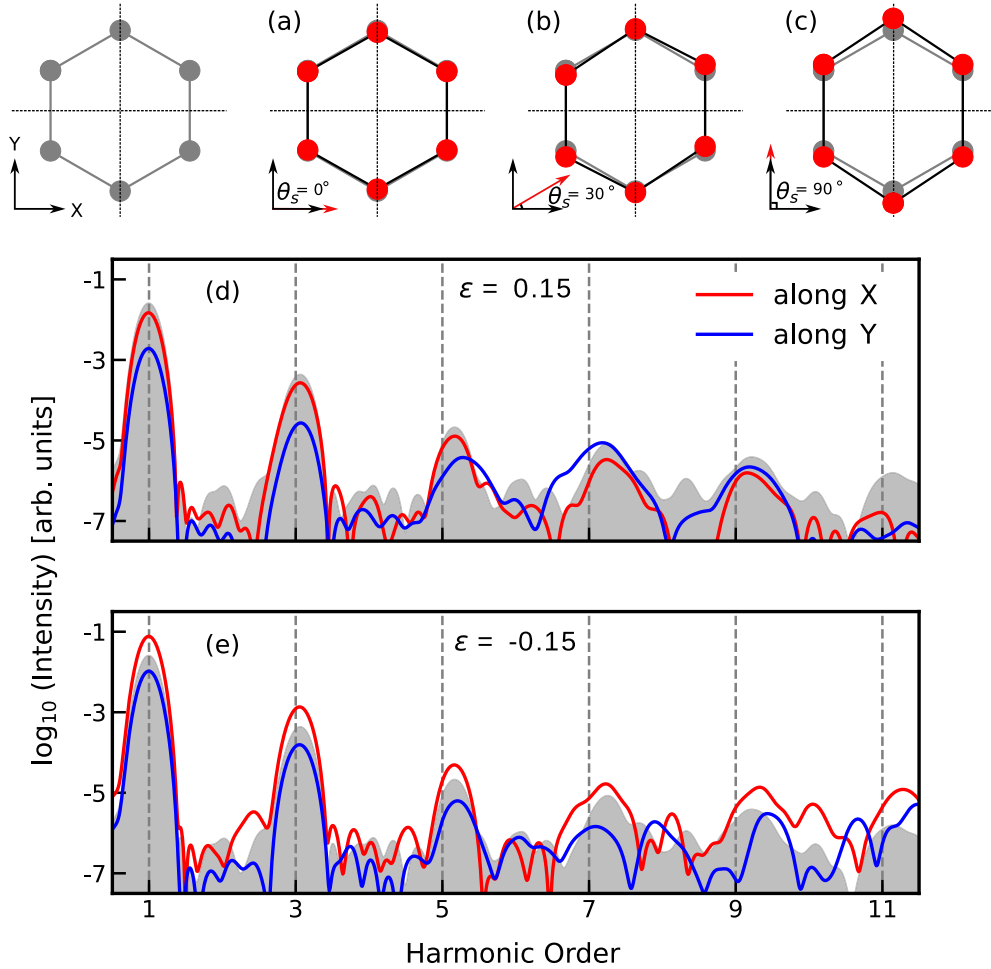


FIG. 1. Real-space structure of the strained graphene when the uniaxial tensile strain is applied along the (a) zigzag, (b)  $30^\circ$ , and (c) armchair directions. The structure of the graphene without strain is shown in gray as a reference structure. High-harmonic spectra of the strained graphene for strain strengths (d)  $\varepsilon = 0.15$  and (e)  $\varepsilon = -0.15$  along  $\theta_s = 30^\circ$ . The red and blue colors stand for the polarization of emitted harmonics along the X (zigzag) and Y (armchair) directions, respectively. The driving laser pulse is polarized along the X direction. The gray-shaded region represents the high-harmonic spectra of unstrained graphene, serving as the reference. The emitted harmonics are polarized along the X direction for unstrained graphene.

a Gaussian function, which is Fourier transformed in time domain and projected in the  $J_x - J_y$  plane. The in-phase relation between the parallel and perpendicular components of the total current, corresponding to H3 and H5 harmonics, causes a rotation of the polarization plane in strained graphene. The rotation of the polarization plane in strained graphene can be attributed to broken reflection symmetries along the XZ and YZ planes, which leads to the generation of the current perpendicular to the driving laser field's polarization. This is analogous to the optical Hall effect [94]. The rotation is in the opposite direction for the tensile and compressive strains, as evident from Figs. 2(a) and 2(d), respectively. Thus, the rotation is sensitive to the nature of the strain.

Reliable information about the strain's direction cannot be extracted exclusively from Figs. 2(a) and 2(d) for the following reasons: Unstrained graphene exhibits  $30^\circ$  and  $90^\circ$  as symmetrically equivalent directions from its sixfold rotational symmetry. This changes for strained graphene. There is no change in the polarization plane when the strain is along  $90^\circ$  due to the presence of reflection plane symmetry [see Fig. 1(c)], which contrasts with the situation when strain is

along  $30^\circ$  for the laser polarized along the X direction [see Fig. 1(b)]. Thus, the extent of the polarization rotation simultaneously depends on the strain's angle and the polarization of the driving pulse. Therefore, it is imperative to analyze the laser polarization direction dependence on the polarization properties of the emitted harmonics.

Figures 2(b) and 2(e) present the polarization dependence of H3 and H5 for  $\varepsilon = 0.15$  and  $\varepsilon = -0.15$  along  $\theta_s = 30^\circ$ , respectively. Both H3 and H5 are highly anisotropic in nature and the maximum yield is sensitive to the direction of the applied strain. On the other hand, the polarization dependence of H3 corresponding to the unstrained graphene is isotropic, whereas H5 exhibits sixfold symmetry as reported earlier [78]. It is striking to observe that the direction of the maximum yield is perpendicular to the direction of the tensile strain. This observation changes when the strain's nature changes from tensile to compressive. The direction of maxima is along the direction of applied strain, as evident from Fig. 2(e). Thus, it can be concluded that the maxima of the harmonic yield align along the direction in which the lattice structure is compressed [see Figs. 1(a)–1(c)]. The principal axis of

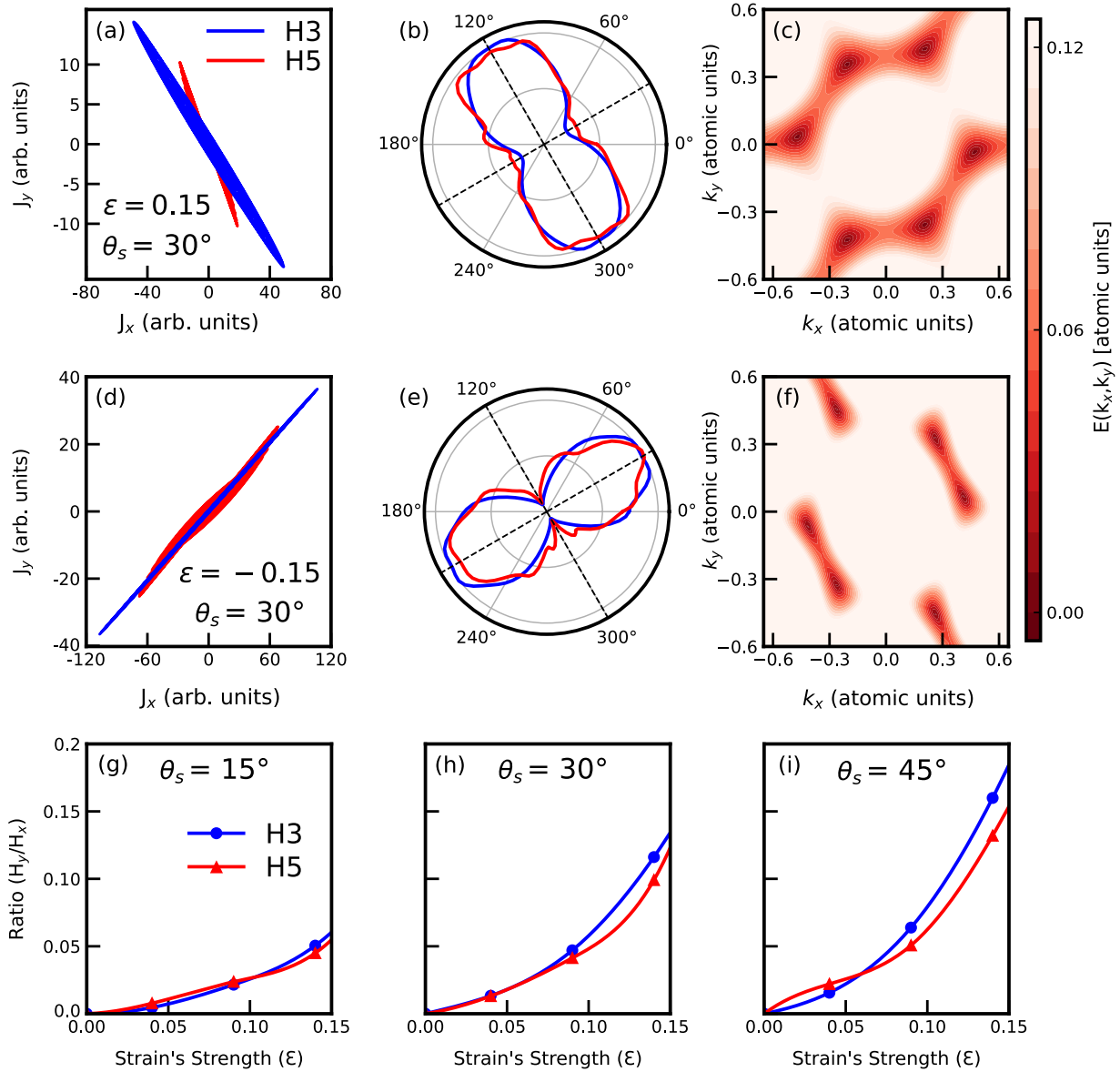


FIG. 2. Projection of the time profile of the third (H3) and fifth (H5) harmonics corresponding to graphene under uniaxial strain with (a)  $\epsilon = 0.15$  and (d)  $\epsilon = -0.15$  along  $\theta_s = 30^\circ$ . Variations in the normalized harmonic yields of H3 and H5 for (b)  $\epsilon = 0.15$  and (e)  $\epsilon = -0.15$  along  $\theta_s = 30^\circ$ . Energy contour of the conduction band of graphene under the uniaxial strain of strength (c)  $\epsilon = 0.15$  and (f)  $\epsilon = -0.15$  along  $\theta_s = 30^\circ$ . The ratio of the perpendicular and parallel components of the total harmonic yield for graphene under different values of  $\epsilon$  along (g)  $\theta_s = 15^\circ$ , (h)  $30^\circ$ , and (i)  $45^\circ$ .

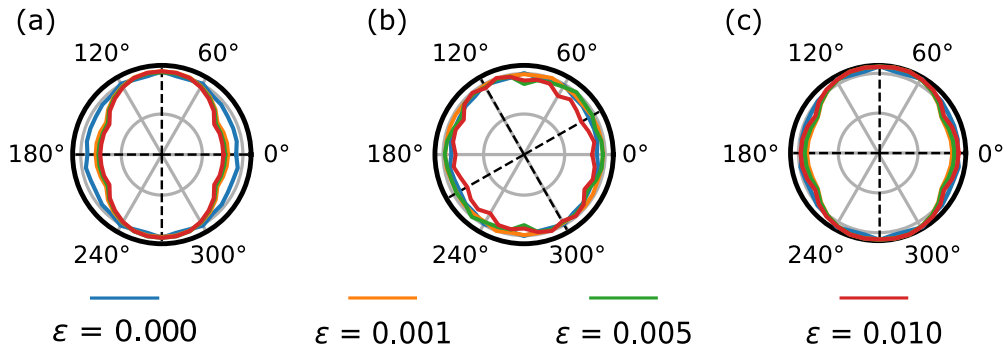


FIG. 3. Polarization dependence on the normalized yield of H3 in strained graphene exposed to different strengths of the tensile uniaxial strain along (a)  $\theta_s = 0^\circ$ , (b)  $30^\circ$ , and (c)  $90^\circ$ .

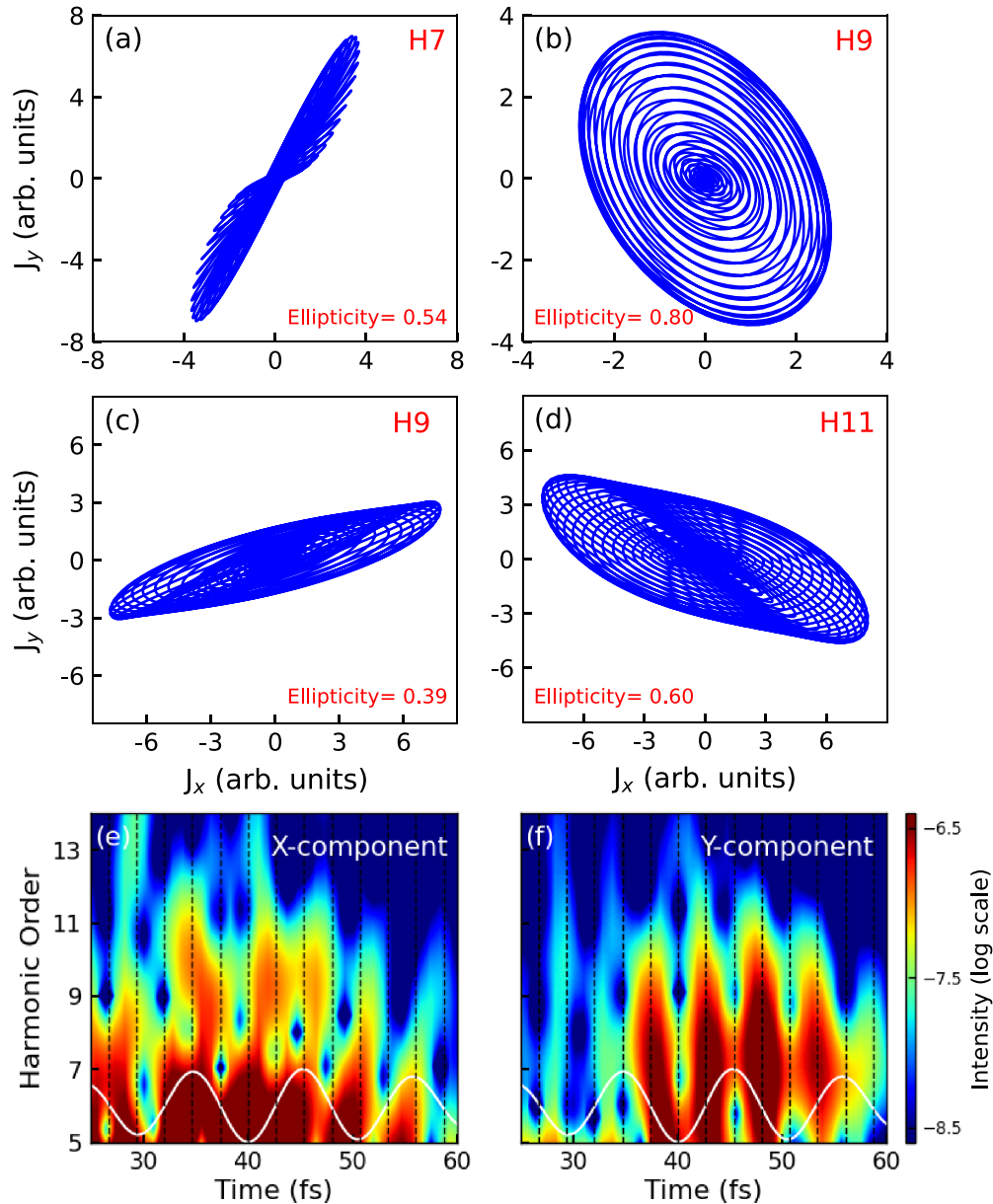


FIG. 4. Projection of time profile of the (a) seventh (H7) and (b) ninth (H9) harmonics of the strained graphene with  $\varepsilon = 0.15$  for  $\theta_s = 30^\circ$ . (c) and (d) Same as (a) and (b), respectively, for ninth (H9) and eleventh (H11) harmonics with  $\varepsilon = -0.15$ . Time-frequency map of the (e) X and (f) Y components of the interband harmonics of the strained graphene with  $\varepsilon = 0.15$  along  $\theta_s = 30^\circ$ . The electric field of the driving laser pulse is shown in white and the black dashed lines correspond to the minima, maxima, and zeros of the electric field.

the unstrained graphene exhibits sixfold symmetry, which reduces to twofold for graphene under uniaxial strain [see Figs. 1(a)–1(c)], resulting in the anisotropic behavior. The modifications in the conduction band in two dimensions corresponding to  $\varepsilon = 0.15$  and  $\varepsilon = -0.15$  are, respectively, shown in Figs. 2(c) and 2(f). The distortions in the band structure drive electrons to different parts of the Brillouin zone depending on the angle and nature of the strain, recording the microscopic structural alterations in the polarization map.

So far, we have discussed results for  $\varepsilon = \pm 0.15$ . Let us investigate how the polarization rotation changes with  $\varepsilon$ . For this purpose, we analyze the ratio of the perpendicular and parallel harmonic yields for different  $\varepsilon$ . Figures 2(g)–2(i) present the ratio for H3 and H5 as a function of  $\varepsilon$  and  $\theta_s$ . It

is interesting to observe that the ratio increases monotonically with  $\varepsilon$ . Moreover, the ratio is also sensitive to  $\theta_s$ . It indicates that the rotation of the polarization plane has a nonlinear increase with  $\varepsilon$  and  $\theta_s$ . Thus, one could qualitatively quantify  $\theta_s$  by analyzing the ratio of the harmonic components.

We further comment on the sensitivity of the polarization rotation with respect to  $\varepsilon$ . It is interesting to observe that the strength as small as  $\varepsilon = 0.01$  results in a significant anisotropic dependence. Moreover, a measurable anisotropy is present even for  $\varepsilon = 0.001$ , which corresponds to a 0.03% change in the lattice parameter (see Fig. 3). Thus, the extent of the anisotropy can be used to quantify the strain's strength. Moreover, the direction and nature of the strain can be extracted from the maxima of the anisotropic yield. It is

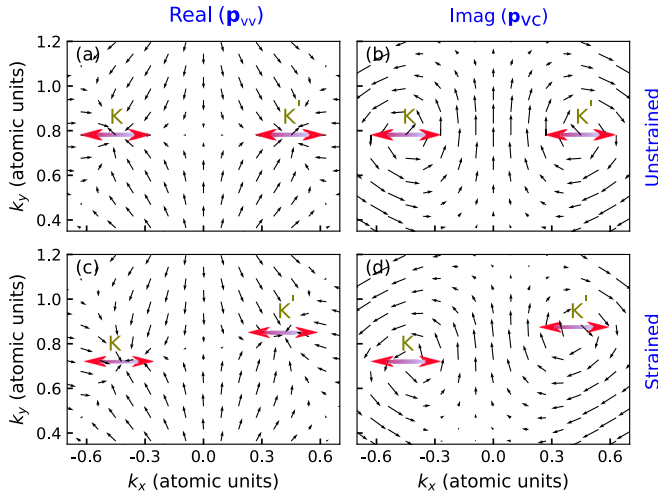


FIG. 5. Diagonal momentum-matrix element of the valence band (band velocity,  $\mathbf{p}_{vv}$ ) of (a) unstrained graphene and (c) strained graphene with  $\epsilon = 0.15$  and  $\theta_s = 30^\circ$ . The off-diagonal momentum-matrix element between the valence and conduction bands ( $\mathbf{p}_{vc}$ ) of (b) unstrained and (d) strained graphene.  $K$  and  $K'$  are high-symmetry points in the Brillouin zone.

interesting to note that the maximum harmonic yield is along the stretching direction when the uniaxial tensile strain is along  $90^\circ$  [Fig. 3(c)]. However, we observe the harmonic yield is peaked along the direction of compression when  $\epsilon$  is greater than 0.02, as presented in the Supplemental Material [93], which is analogous to Fig. 2(b).

Let us shift our attention toward the properties of the higher-order harmonics. Figures 4(a) and 4(b) display the temporal profiles of the seventh (H7) and ninth (H9) harmonics of strained graphene with  $\epsilon = 0.15$  along  $\theta_s = 30^\circ$ , respectively. In contrast to the linear polarization of H3 and H5, H7 and H9 are elliptical, as evident from the figure. Similarly, the ninth (H9) and eleventh (H11) harmonics of the strained graphene, with  $\epsilon = -0.15$  along  $\theta_s = 30^\circ$ , are elliptical, as reflected from Figs. 4(c) and 4(d), respectively. It is fascinating to note that the polarization properties of the harmonics are contrasting in the lower and higher orders in strained graphene. In the lower orders, we only observed a rotation of the polarization plane of the emitted harmonics. On the other hand, we observe an out-of-phase relation in the parallel and perpendicular components, resulting in the elliptically polarized higher-order harmonics.

To have a better understanding of the unusual polarization of higher-order harmonics, let us analyze the time-frequency map of the harmonics of the strained graphene with  $\epsilon = 0.15$  along  $\theta_s = 30^\circ$ . The time-frequency map of the HHG is obtained via Gabor transformation as [95]

$$G(\omega, t) = \int dt' \frac{\exp[-(t-t')^2/2\zeta^2]}{\sqrt{2\pi}\zeta} \mathbf{J}(t') \exp(i\omega t'), \quad (4)$$

where  $\zeta = 1/(3\omega)$  is considered to obtain an adequate balance between the time and energy resolutions. Analysis of the time-frequency map of the X component of the interband harmonics indicates that the harmonic bursts are around the crest and trough of the electric field, as evident from Fig. 4(e). On the

other hand, the Y component demonstrates that the harmonic bursts occur around the zeros of the electric field, as reflected from Fig. 4(f). Thus, an out-of-phase relation between the X and Y components is observed, indicating different underlying mechanisms of the electron dynamics.

Let us further delve into the physical process responsible for the anisotropic and unusual polarization dependence. It is known that the polarization properties of the emitted harmonics strongly depend on the nature of the underlying electron dynamics [96]. An intricate interplay of the interband and intraband contributions in higher-order harmonic generation in graphene was previously shown [78]. In the following part, we explain the unusual polarization properties of higher-order harmonics in strained graphene by analyzing the interband and intraband components of the harmonics.

The density-matrix element ( $\rho_{mn}^k$ ) and momentum-matrix element ( $\mathbf{p}_{mn}^k$ ) are related to  $\mathbf{J}(t)$  as

$$\begin{aligned} \mathbf{J}(t) &\propto \sum_{m \neq n, \mathbf{k}} \rho_{mn}^{\mathbf{k}}(t) \mathbf{p}_{nm}^{\mathbf{k}+\mathbf{A}(t)} + \sum_{m, \mathbf{k}} \rho_{mm}^{\mathbf{k}}(t) \mathbf{p}_{mm}^{\mathbf{k}+\mathbf{A}(t)} \\ &= \mathbf{J}_{\text{inter}}(t) + \mathbf{J}_{\text{intra}}(t). \end{aligned} \quad (5)$$

Here,  $\mathbf{A}(t)$  is the vector potential of the laser field.  $\mathbf{J}_{\text{inter}}(t)$  and  $\mathbf{J}_{\text{intra}}(t)$  are the interband and intraband currents, respectively. The ultrafast electron dynamics can be through either of these contributions.

The diagonal and off-diagonal components of the momentum-matrix element are shown in Fig. 5. The diagonal elements of the momentum-matrix element are the band velocities, and the off-diagonal elements are proportional to the dipole coupling. Note that according to the semiclassical description of the electron dynamics, the intraband current is proportional to the group velocity and Berry curvature. Strained graphene exhibits inversion and time-reversal symmetries, and therefore Berry curvature is zero. Another consequence of having these symmetries is pure imaginary off-diagonal momentum-matrix elements [Figs. 5(b) and 5(d)].

It is evident that the off-diagonal momentum-matrix elements close to distinct  $K$  points have opposite chirality [see Fig. 5(b)]. Thus, the interband currents generated close to different  $K$  points are out of phase and interfere destructively. Also, the available joint density of states for interband transitions are less in the lower-energy response [78]. So, the lower-order harmonics are dominantly from the intraband contributions, which constructively interfere from  $K$  and  $K'$  regions, as evident from Fig. 5(a). The unstrained graphene favors the parallel component of the intraband current, apparent from the symmetries of the band velocity [see the reflection symmetry with respect to the X axis for Y components of the vector field in Fig. 5(a)]. In strained graphene, the reflection planes are broken and the vector field is distorted [see Fig. 5(c)], resulting in the perpendicular component of the intraband current. As the parallel and perpendicular currents are generated from the same underlying mechanism, they are in phase, resulting in the rotation of the plane of polarization of the lower-order harmonics (see Figs. 6 and 7). Moreover, these distortions in the band velocities are responsible for the characteristic polarization dependence observed in Fig. 2(b).

When electrons are excited away from  $K$  points along the laser polarization direction, they result in a perpendicular

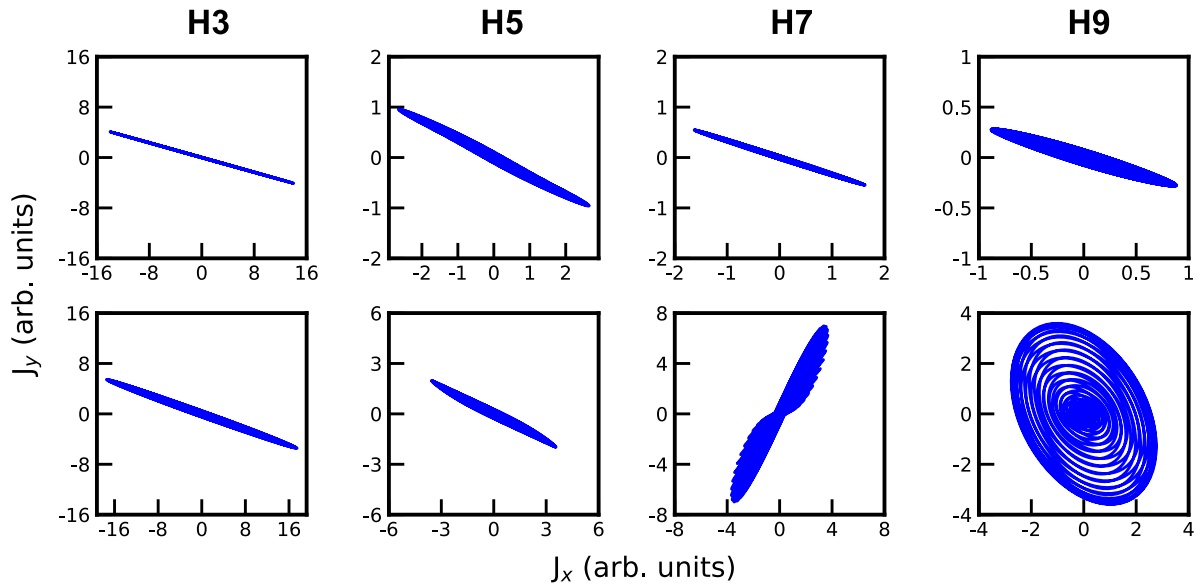


FIG. 6. Projections of the time profile of H3, H5, H7, and H9 of strained graphene with  $\varepsilon = 0.15$  along  $\theta_s = 30^\circ$ . The upper panel shows the harmonics generated solely by the intraband current, whereas the lower panel displays the harmonics resulting from the combined interband and intraband currents.

contribution of interband current [Figs. 5(b) and 5(d)]. However, the perpendicular component in unstrained graphene cancels among different  $K$  points due to the symmetries of the vector field [Fig. 5(b)]. Since the symmetry planes are absent in strained graphene, a net perpendicular interband current is generated from the distorted vector field [Fig. 5(d)]. It is essential to consider that the parallel and perpendicular current contributions happen from different regions in the Brillouin zone [see the modification in the  $Y$  component of the momentum-matrix elements throughout the Brillouin zone in Figs. 5(c) and 5(d)]. So, different nonlinear processes contribute in the parallel and perpendicular directions. The interference of different nonlinear processes can result in different time-frequency maps in the orthogonal directions,

generating a phase difference and resulting in elliptical harmonics. In short, this nontrivial interplay of intraband and interband currents in the parallel and perpendicular directions is responsible for the elliptical higher-order harmonics as observed in Figs. 4(a)–4(d).

Before concluding, let us further analyze the time profiles the harmonics solely originated by intraband and combined interband and intraband currents in Figs. 6 and 7 for  $\varepsilon = 0.15$  and  $-0.15$  along  $\theta_s = 30^\circ$ , respectively. As discussed earlier, the intraband contribution leads to the rotation of the polarization plane of the lower-order harmonics. On the other hand, the significant contribution from the interband dynamics, along with the intraband current, results in elliptically polarized higher-order harmonics.

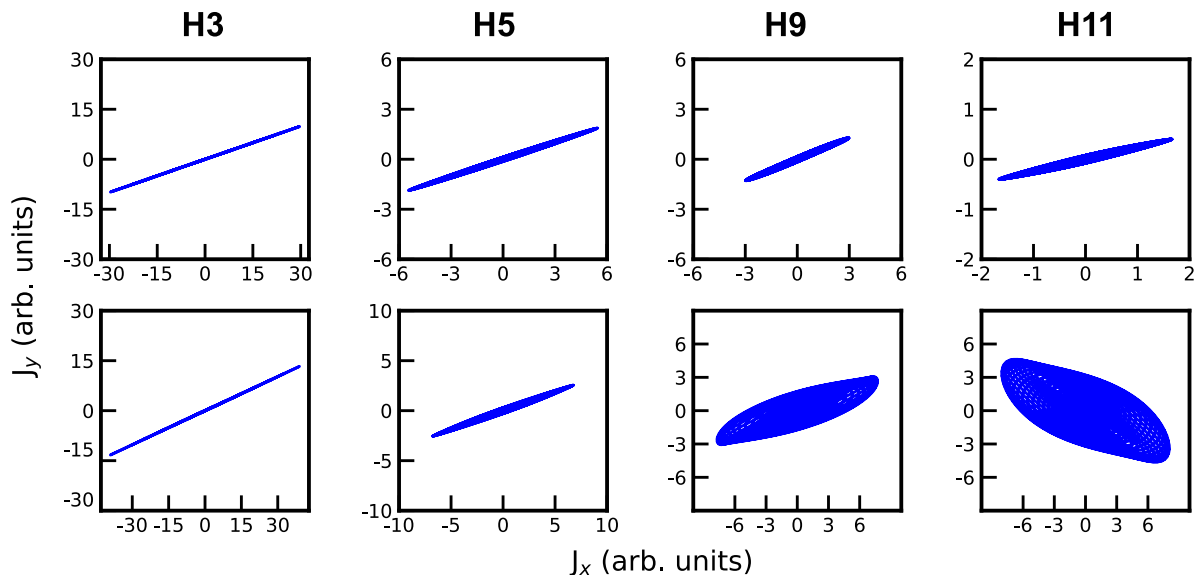


FIG. 7. Same as Fig. 6, for H3, H5, H9, and H11 for the applied strain of  $\varepsilon = -0.15$  along  $\theta_s = 30^\circ$ .

#### IV. CONCLUSION

To summarize, we have unequivocally demonstrated how the analysis of the polarization dependence of the emitted harmonics can be used to quantify both the qualitative and quantitative nature of the strain in graphene. It is observed that the uniaxial strain in graphene drastically affects the harmonic generation. In addition, tensile and compressive uniaxial strains influence the generation process differently. The absence of the reflection symmetries in strained graphene leads to the generation of harmonics perpendicular to the incident laser pulse. The X and Y components of the lower-order harmonics are in phase, which results in rotation of the polarization plane—analogueous to the optical Hall effect. The extent of the rotation depends on the angle at which the strain is present, and exhibits a nonlinear scaling with the strain's strength. Higher-order harmonics have an intricate interplay of the interband and intraband contributions. The X and Y components of the higher-order harmonics are in

an out-of-phase relation, which leads to the generation of elliptically or circularly polarized harmonics. Our findings add a different dimension to high-harmonic spectroscopy by establishing sensitivity toward strain, which will have important technological fall-outs while designing and characterizing 2D materials-based engineered devices where strain is unavoidable [97–99]. Moreover, controlling the properties of engineered graphene allows us to tailor the polarization of emitted harmonics from linear to elliptical, which will be useful to interrogate numerous chiral-sensitive light-matter interactions on an ultrafast timescale.

#### ACKNOWLEDGMENTS

We acknowledge fruitful discussions with M. Ivanov (MBI, Berlin), D. Reis (SLAC, USA), A. Kanda (Tsukuba University), and S. Pujari (IITB). G.D. acknowledges financial support from SERB India (Project No. MTR/2021/000138).

- 
- [1] S. Ghimire, A. D. DiChiara, E. Sistrunk, P. Agostini, L. F. DiMauro, and D. A. Reis, Observation of high-order harmonic generation in a bulk crystal, *Nat. Phys.* **7**, 138 (2011).
  - [2] S. Ghimire and D. A. Reis, High-harmonic generation from solids, *Nat. Phys.* **15**, 10 (2019).
  - [3] E. Goulielmakis and T. Brabec, High harmonic generation in condensed matter, *Nat. Photon.* **16**, 411 (2022).
  - [4] T. T. Luu, M. Garg, S. Yu. Kruchinin, A. Moulet, M. Th. Hassan, and E. Goulielmakis, Extreme ultraviolet high-harmonic spectroscopy of solids, *Nature (London)* **521**, 498 (2015).
  - [5] M. Hohenleutner, F. Langer, O. Schubert, M. Knorr, U. Huttner, S. W. Koch, M. Kira, and R. Huber, Real-time observation of interfering crystal electrons in high-harmonic generation, *Nature (London)* **523**, 572 (2015).
  - [6] F. Langer, C. P. Schmid, S. Schlauderer, M. Gmitra, J. Fabian, P. Nagler, C. Schüller, T. Korn, P. G. Hawkins, J. T. Steiner, U. Huttner, S. W. Koch, M. Kira, and R. Huber, Lightwave valleytronics in a monolayer of tungsten diselenide, *Nature (London)* **557**, 76 (2018).
  - [7] M. S. Mrudul, A. Pattanayak, M. Ivanov, and G. Dixit, Direct numerical observation of real-space recollision in high-order harmonic generation from solids, *Phys. Rev. A* **100**, 043420 (2019).
  - [8] S. Imai, A. Ono, and S. Ishihara, High harmonic generation in a correlated electron system, *Phys. Rev. Lett.* **124**, 157404 (2020).
  - [9] M. Borsch, C. P. Schmid, L. Weigl, S. Schlauderer, N. Hofmann, C. Lange, J. T. Steiner, S. W. Koch, R. Huber, and M. Kira, Super-resolution lightwave tomography of electronic bands in quantum materials, *Science* **370**, 1204 (2020).
  - [10] A. Pattanayak, S. Pujari, and G. Dixit, Role of Majorana fermions in high-harmonic generation from Kitaev chain, *Sci. Rep.* **12**, 6722 (2022).
  - [11] G. Vampa, T. J. Hammond, N. Thiré, B. E. Schmidt, F. Légaré, C. R. McDonald, T. Brabec, D. D. Klug, and P. B. Corkum, All-optical reconstruction of crystal band structure, *Phys. Rev. Lett.* **115**, 193603 (2015).
  - [12] C. P. Schmid, L. Weigl, P. Grössing, V. Junk, C. Gorini, S. Schlauderer, S. Ito, M. Meierhofer, N. Hofmann, D. Afanasiev *et al.*, Tunable noninteger high-harmonic generation in a topological insulator, *Nature (London)* **593**, 385 (2021).
  - [13] C. Qian, C. Yu, S. Jiang, T. Zhang, J. Gao, S. Shi, H. Pi, H. Weng, and R. Lu, Role of shift vector in high-harmonic generation from noncentrosymmetric topological insulators under strong laser fields, *Phys. Rev. X* **12**, 021030 (2022).
  - [14] N. Rana and G. Dixit, Probing phonon-driven symmetry alterations in graphene via high-order-harmonic spectroscopy, *Phys. Rev. A* **106**, 053116 (2022).
  - [15] R. E. F. Silva, I. V. Blinov, A. N. Rubtsov, O. Smirnova, and M. Ivanov, High-harmonic spectroscopy of ultrafast many-body dynamics in strongly correlated systems, *Nat. Photon.* **12**, 266 (2018).
  - [16] A. Bharti, M. S. Mrudul, and G. Dixit, High-harmonic spectroscopy of light-driven nonlinear anisotropic anomalous Hall effect in a Weyl semimetal, *Phys. Rev. B* **105**, 155140 (2022).
  - [17] H. Liu, Y. Li, Y. S. You, S. Ghimire, T. F. Heinz, and D. A. Reis, High-harmonic generation from an atomically thin semiconductor, *Nat. Phys.* **13**, 262 (2017).
  - [18] C. Heide, Y. Kobayashi, D. R. Baykusheva, D. Jain, J. A. Sobota, M. Hashimoto, P. S. Kirchmann, S. Oh, T. F. Heinz, D. A. Reis *et al.*, Probing topological phase transitions using high-harmonic generation, *Nat. Photon.* **16**, 620 (2022).
  - [19] C. R. McDonald, K. S. Amin, S. Aalmalki, and T. Brabec, Enhancing high harmonic output in solids through quantum confinement, *Phys. Rev. Lett.* **119**, 183902 (2017).
  - [20] M. S. Mrudul, N. Tancogne-Dejean, A. Rubio, and G. Dixit, High-harmonic generation from spin-polarized defects in solids, *npj Comput. Mater.* **6**, 10 (2020).
  - [21] H. Liu, C. Guo, G. Vampa, J. L. Zhang, T. Sarmiento, M. Xiao, P. H. Bucksbaum, J. Vučković, S. Fan, and D. A. Reis, Enhanced high-harmonic generation from an all-dielectric metasurface, *Nat. Phys.* **14**, 1006 (2018).
  - [22] M. R. Shcherbakov, H. Zhang, M. Tripepi, G. Sartorello, N. Talisa, A. AlShafey, Z. Fan, J. Twardowski, L. A. Krivitsky,

- A. I. Kuznetsov *et al.*, Generation of even and odd high harmonics in resonant metasurfaces using single and multiple ultra-intense laser pulses, *Nat. Commun.* **12**, 4185 (2021).
- [23] A. Pattanayak, M. S. Mrudul, and G. Dixit, Influence of vacancy defects in solid high-order harmonic generation, *Phys. Rev. A* **101**, 013404 (2020).
- [24] A. Ferré, C. Handschin, M. Dumergue, F. Burgy, A. Comby, D. Descamps, B. Fabre, G. A. Garcia, R. Géneaux, L. Merceron, E. Mevel, L. Nahon, S. Petit, B. Pons, D. Staedter, S. Weber, T. Ruchon, V. Blanchet, and Y. Mairesse, A table-top ultrashort light source in the extreme ultraviolet for circular dichroism experiments, *Nat. Photon.* **9**, 93 (2015).
- [25] O. Kfir, P. Grychtol, E. Turgut, R. Knut, D. Zusin, D. Popmintchev, T. Popmintchev, H. Nembach, J. M. Shaw, A. Fleischer, H. Kapteyn, M. Murnane, and O. Cohen, Generation of bright phase-matched circularly-polarized extreme ultraviolet high harmonics, *Nat. Photon.* **9**, 99 (2015).
- [26] C. Boeglin, E. Beaurepaire, V. Halté, V. López-Flores, C. Stamm, N. Pontius, H. A. Dürr, and J. Y. Bigot, Distinguishing the ultrafast dynamics of spin and orbital moments in solids, *Nature (London)* **465**, 458 (2010).
- [27] S. Giri, A. M. Dudzinski, J. C. Tremblay, and G. Dixit, Time-dependent electronic current densities in chiral molecules, *Phys. Rev. A* **102**, 063103 (2020).
- [28] I. Radu, K. Vahaplar, C. Stamm, T. Kachel, N. Pontius, H. A. Dürr, T. A. Ostler, J. Barker, R. F. L. Evans, R. W. Chantrell, A. Tsukamoto, A. Itoh, A. Kirilyuk, T. Rasing, and A. V. Kimel, Transient ferromagnetic-like state mediating ultrafast reversal of antiferromagnetically coupled spins, *Nature (London)* **472**, 205 (2011).
- [29] R. Cireasa, A. E. Boguslavskiy, B. Pons, M. C. H. Wong, D. Descamps, S. Petit, H. Ruf, N. Thiré, A. Ferré, J. Suarez, J. Higué, B. E. Schmidt, A. F. Alharbi, F. Legare, V. Blanchet, B. Fabre, S. Patchkovskii, O. Smirnova, Y. Mairesse, and V. R. Bhardwaj, Probing molecular chirality on a sub-femtosecond timescale, *Nat. Phys.* **11**, 654 (2015).
- [30] K. S. Novoselov, A. K. Geim, S. V. Morozov, D. Jiang, Y. Zhang, S. V. Dubonos, I. V. Grigorieva, and A. A. Firsov, Electric field effect in atomically thin carbon films, *Science* **306**, 666 (2004).
- [31] S. Manzeli, D. Ovchinnikov, D. Pasquier, O. V. Yazyev, and A. Kis, 2D transition metal dichalcogenides, *Nat. Rev. Mater.* **2**, 17033 (2017).
- [32] F. Bonaccorso, Z. Sun, T. Hasan, and A. C. Ferrari, Graphene photonics and optoelectronics, *Nat. Photon.* **4**, 611 (2010).
- [33] A. R. Khan, L. Zhang, K. Ishaq, A. Ikram, T. Yildirim, B. Liu, S. Rahman, and Y. Lu, Optical harmonic generation in 2D materials, *Adv. Funct. Mater.* **32**, 2105259 (2022).
- [34] N. Rana and G. Dixit, All-optical ultrafast valley switching in two-dimensional materials, *Phys. Rev. Appl.* **19**, 034056 (2023).
- [35] A. Chaves, J. G. Azadani, H. Alsalman, D. R. Da Costa, R. Frisenda, A. J. Chaves, S. H. Song, Y. D. Kim, D. He, J. Zhou *et al.*, Bandgap engineering of two-dimensional semiconductor materials, *npj 2D Mater. Appl.* **4**, 29 (2020).
- [36] Z. Peng, X. Chen, Y. Fan, D. J. Srolovitz, and D. Lei, Strain engineering of 2D semiconductors and graphene: From strain fields to band-structure tuning and photonic applications, *Light: Sci. Appl.* **9**, 190 (2020).
- [37] Z. Dai, L. Liu, and Z. Zhang, Strain engineering of 2D materials: Issues and opportunities at the interface, *Adv. Mater.* **31**, 1805417 (2019).
- [38] R. Roldán, A. Castellanos-Gomez, E. Cappelluti, and F. Guinea, Strain engineering in semiconducting two-dimensional crystals, *J. Phys.: Condens. Matter* **27**, 313201 (2015).
- [39] T. Roy, M. Tosun, J. S. Kang, A. B. Sachid, S. B. Desai, M. Hettick, C. C. Hu, and A. Javey, Field-effect transistors built from all two-dimensional material components, *ACS Nano* **8**, 6259 (2014).
- [40] F. Schwierz, J. Pezoldt, and R. Granzner, Two-dimensional materials and their prospects in transistor electronics, *Nanoscale* **7**, 8261 (2015).
- [41] N. J. G. Couto, D. Costanzo, S. Engels, D.-K. Ki, K. Watanabe, T. Taniguchi, C. Stampfer, F. Guinea, and A. F. Morpurgo, Random strain fluctuations as dominant disorder source for high-quality on-substrate graphene devices, *Phys. Rev. X* **4**, 041019 (2014).
- [42] M. A. Bissett, M. Tsuji, and H. Ago, Strain engineering the properties of graphene and other two-dimensional crystals, *Phys. Chem. Chem. Phys.* **16**, 11124 (2014).
- [43] B. Amorim, A. Cortijo, F. De Juan, A. G. Grushin, F. Guinea, A. Gutiérrez-Rubio, H. Ochoa, V. Parente, R. Roldán, P. San-Jose *et al.*, Novel effects of strains in graphene and other two-dimensional materials, *Phys. Rep.* **617**, 1 (2016).
- [44] C. Galiotis, O. Frank, E. N. Koukaras, and D. Sfyris, Graphene mechanics: Current status and perspectives, *Annu. Rev. Chem. Biomol. Eng.* **6**, 121 (2015).
- [45] F. Guinea, M. I. Katsnelson, and A. K. Geim, Energy gaps and a zero-field quantum Hall effect in graphene by strain engineering, *Nat. Phys.* **6**, 30 (2010).
- [46] C. Si, Z. Sun, and F. Liu, Strain engineering of graphene: A review, *Nanoscale* **8**, 3207 (2016).
- [47] O. Frank, G. Tsoukleri, I. Riaz, K. Papagelis, J. Parthenios, A. C. Ferrari, A. K. Geim, K. S. Novoselov, and C. Galiotis, Development of a universal stress sensor for graphene and carbon fibres, *Nat. Commun.* **2**, 255 (2011).
- [48] T.-J. Shao, Y. Xu, X.-H. Huang, and X.-B. Bian, Strain effects on high-order harmonic generation in solids, *Phys. Rev. A* **99**, 013432 (2019).
- [49] M.-X. Guan, C. Lian, S.-Q. Hu, H. Liu, S.-J. Zhang, J. Zhang, and S. Meng, Cooperative evolution of intraband and interband excitations for high-harmonic generation in strained MoS<sub>2</sub>, *Phys. Rev. B* **99**, 184306 (2019).
- [50] X.-S. Kong, X.-Y. Wu, L. Geng, and W.-D. Yu, Strain effects on high-harmonic generation in monolayer hexagonal boron nitride, *Front. Phys.* **10**, 1032671 (2022).
- [51] R. Qin and Z.-Yu Chen, Strain-controlled high harmonic generation with Dirac fermions in silicene, *Nanoscale* **10**, 22593 (2018).
- [52] N. N. Klimov, S. Jung, S. Zhu, T. Li, C. A. Wright, S. D. Solares, D. B. Newell, N. B. Zhitenev, and J. A. Stroschio, Electromechanical properties of graphene drumheads, *Science* **336**, 1557 (2012).
- [53] J. S. Bunch, S. S. Verbridge, J. S. Alden, A. M. Van Der Zande, J. M. Parpia, H. G. Craighead, and P. L. McEuen, Impermeable atomic membranes from graphene sheets, *Nano Lett.* **8**, 2458 (2008).

- [54] C. Lee, X. Wei, J. W. Kysar, and J. Hone, Measurement of the elastic properties and intrinsic strength of monolayer graphene, *Science* **321**, 385 (2008).
- [55] F. Guinea, Strain engineering in graphene, *Solid State Commun.* **152**, 1437 (2012).
- [56] Y. Zhang, Y. Jin, J. Liu, Q. Ren, Z. Chen, Y. Zhao, and P. Zhao, Strain engineering of graphene on rigid substrates, *Nanoscale Adv.* **4**, 5056 (2022).
- [57] H. Tomori, A. Kanda, H. Goto, Y. Ootuka, K. Tsukagoshi, S. Moriyama, E. Watanabe, and D. Tsuya, Introducing nonuniform strain to graphene using dielectric nanopillars, *Appl. Phys. Express* **4**, 075102 (2011).
- [58] W. Bao, F. Miao, Z. Chen, H. Zhang, W. Jang, C. Dames, and C. N. Lau, Controlled ripple texturing of suspended graphene and ultrathin graphite membranes, *Nat. Nanotechnol.* **4**, 562 (2009).
- [59] M. Huang, H. Yan, C. Chen, D. Song, T. F. Heinz, and J. Hone, Phonon softening and crystallographic orientation of strained graphene studied by raman spectroscopy, *Proc. Natl. Acad. Sci. USA* **106**, 7304 (2009).
- [60] A. C. Ferrari and D. M. Basko, Raman spectroscopy as a versatile tool for studying the properties of graphene, *Nat. Nanotechnol.* **8**, 235 (2013).
- [61] J.-B. Wu, M.-L. Lin, X. Cong, H.-N. Liu, and P.-H. Tan, Raman spectroscopy of graphene-based materials and its applications in related devices, *Chem. Soc. Rev.* **47**, 1822 (2018).
- [62] E. del Corro, L. Kavan, M. Kalbac, and O. Frank, Strain assessment in graphene through the raman 2D mode, *J. Phys. Chem. C* **119**, 25651 (2015).
- [63] H. Tomori, K. Nakamura, and A. Kanda, Improved method for determining crystallographic orientation of strained graphene by Raman spectroscopy, *Appl. Phys. Express* **13**, 075006 (2020).
- [64] N. Yoshikawa, T. Tamaya, and K. Tanaka, High-harmonic generation in graphene enhanced by elliptically polarized light excitation, *Science* **356**, 736 (2017).
- [65] M. Taucer, T. J. Hammond, P. B. Corkum, G. Vampa, C. Couture, N. Thiré, B. E. Schmidt, F. Légaré, H. Selvi, N. Unsuré *et al.*, Nonperturbative harmonic generation in graphene from intense midinfrared pulsed light, *Phys. Rev. B* **96**, 195420 (2017).
- [66] S. Cha, M. Kim, Y. Kim, S. Choi, S. Kang, H. Kim, S. Yoon, G. Moon, T. Kim, Y. W. Lee *et al.*, Gate-tunable quantum pathways of high harmonic generation in graphene, *Nat. Commun.* **13**, 6630 (2022).
- [67] H. K. Avetissian, G. F. Mkrtchian, and A. Knorr, Efficient high-harmonic generation in graphene with two-color laser field at orthogonal polarization, *Phys. Rev. B* **105**, 195405 (2022).
- [68] M. S. Mrudul and G. Dixit, Controlling valley-polarization in graphene via tailored light pulses, *J. Phys. B: At. Mol. Opt. Phys.* **54**, 224001 (2021).
- [69] Y. Murakami and M. Schüler, Doping and gap size dependence of high-harmonic generation in graphene: Importance of consistent formulation of light-matter coupling, *Phys. Rev. B* **106**, 035204 (2022).
- [70] F. Dong, Q. Xia, and J. Liu, Ellipticity of the harmonic emission from graphene irradiated by a linearly polarized laser, *Phys. Rev. A* **104**, 033119 (2021).
- [71] Y. Zhang, L. Li, J. Li, T. Huang, P. Lan, and P. Lu, Orientation dependence of high-order harmonic generation in graphene, *Phys. Rev. A* **104**, 033110 (2021).
- [72] R. Boyero-García, A. García-Cabrera, O. Zurrón-Cifuentes, C. Hernández-García, and L. Plaja, Nonclassical high harmonic generation in graphene driven by linearly-polarized laser pulses, *Opt. Express* **30**, 15546 (2022).
- [73] Z. Guan, Z. Yin, J. You, B. Wang, X. Li, G.-L. Wang, X.-X. Zhou, and C. Jin, Optimal generation and systematic analysis of tunable terahertz emissions from single-layer graphene using two-color laser pulses with different durations, *Phys. Rev. A* **108**, 023515 (2023).
- [74] N. Rana, M. S. Mrudul, D. Kartashov, M. Ivanov, and G. Dixit, High-harmonic spectroscopy of coherent lattice dynamics in graphene, *Phys. Rev. B* **106**, 064303 (2022).
- [75] F. Dong and J. Liu, Knee structure in the laser-intensity dependence of harmonic generation for graphene, *Phys. Rev. A* **106**, 043103 (2022).
- [76] Ó. Zurrón-Cifuentes, R. Boyero-García, C. Hernández-García, A. Picón, and L. Plaja, Optical anisotropy of nonperturbative high-order harmonic generation in gapless graphene, *Opt. Express* **27**, 7776 (2019).
- [77] Ó. Zurrón, A. Picón, and L. Plaja, Theory of high-order harmonic generation for gapless graphene, *New J. Phys.* **20**, 053033 (2018).
- [78] M. S. Mrudul and G. Dixit, High-harmonic generation from monolayer and bilayer graphene, *Phys. Rev. B* **103**, 094308 (2021).
- [79] C. Liu, Y. Zheng, Z. Zeng, and R. Li, Driving-laser ellipticity dependence of high-order harmonic generation in graphene, *Phys. Rev. A* **97**, 063412 (2018).
- [80] S. A. Sørngård, S. I. Simonsen, and J. P. Hansen, High-order harmonic generation from graphene: Strong attosecond pulses with arbitrary polarization, *Phys. Rev. A* **87**, 053803 (2013).
- [81] K. L. Ishikawa, Nonlinear optical response of graphene in time domain, *Phys. Rev. B* **82**, 201402(R) (2010).
- [82] L. A. Chizhova, F. Libisch, and J. Burgdörfer, Nonlinear response of graphene to a few-cycle terahertz laser pulse: Role of doping and disorder, *Phys. Rev. B* **94**, 075412 (2016).
- [83] S. A. Mikhailov, Nonlinear electromagnetic response of graphene, *Europhys. Lett.* **79**, 27002 (2007).
- [84] H. K. Avetissian, A. K. Avetissian, G. F. Mkrtchian, and K. V. Sedrakian, Creation of particle-hole superposition states in graphene at multiphoton resonant excitation by laser radiation, *Phys. Rev. B* **85**, 115443 (2012).
- [85] N. Rana, M. S. Mrudul, and G. Dixit, Generation of circularly polarized high harmonics with identical helicity in two-dimensional materials, *Phys. Rev. Appl.* **18**, 064049 (2022).
- [86] H. K. Avetissian and G. F. Mkrtchian, Impact of electron-electron Coulomb interaction on the high harmonic generation process in graphene, *Phys. Rev. B* **97**, 115454 (2018).
- [87] T. Tamaya, H. Akiyama, and T. Kato, Shear-strain controlled high-harmonic generation in graphene, *Phys. Rev. B* **107**, L081405 (2023).
- [88] V. M. Pereira, A. H. C. Neto, and N. M. R. Peres, Tight-binding approach to uniaxial strain in graphene, *Phys. Rev. B* **80**, 045401 (2009).
- [89] O. L. Blakslee, D. G. Proctor, E. J. Seldin, G. B. Spence, and T. Weng, Elastic constants of compression-annealed pyrolytic graphite, *J. Appl. Phys.* **41**, 3373 (1970).

- [90] S. Reich, J. Maultzsch, C. Thomsen, and P. Ordejon, Tight-binding description of graphene, *Phys. Rev. B* **66**, 035412 (2002).
- [91] G. G. Naumis, S. Barraza-Lopez, M. Oliva-Leyva, and H. Terrones, Electronic and optical properties of strained graphene and other strained 2D materials: A review, *Rep. Prog. Phys.* **80**, 096501 (2017).
- [92] M. S. Mrudul, Á. Jiménez-Galán, M. Ivanov, and G. Dixit, Light-induced valleytronics in pristine graphene, *Optica* **8**, 422 (2021).
- [93] See Supplemental Material at <http://link.aps.org/supplemental/10.1103/PhysRevB.110.054103> for the rotation of the polarization plane of harmonics for different dephasing times, polarization dependence of the normalized harmonic yield for different strain strengths, and contributions of inter- and intraband current in graphene under tensile and compressive strains along  $\theta_s = 30^\circ$ .
- [94] V. H. Nguyen, A. Lherbier, and J.-C. Charlier, Optical Hall effect in strained graphene, *2D Mater.* **4**, 025041 (2017).
- [95] I. N. Ansari, M. S. Mrudul, M. F. Ciappina, M. Lewenstein, and G. Dixit, Simultaneous control of harmonic yield and energy cutoff of high-order harmonic generation using seeded plasmonically enhanced fields, *Phys. Rev. A* **98**, 063406 (2018).
- [96] N. Tancogne-Dejean, O. D. Mücke, F. X. Kärtner, and A. Rubio, Ellipticity dependence of high-harmonic generation in solids originating from coupled intraband and interband dynamics, *Nat. Commun.* **8**, 745 (2017).
- [97] M. Sivis, M. Taucer, G. Vampa, K. Johnston, A. Staudte, A. Yu Naumov, D. M. Villeneuve, C. Ropers, and P. B. Corkum, Tailored semiconductors for high-harmonic optoelectronics, *Science* **357**, 303 (2017).
- [98] A. Korobenko, S. Rashid, C. Heide, A. Yu Naumov, D. A. Reis, P. Berini, P. B. Corkum, and G. Vampa, *In situ* nanoscale focusing of extreme ultraviolet solid-state high harmonics, *Phys. Rev. X* **12**, 041036 (2022).
- [99] S. D. C. R. Abbing, R. Kolkowski, Z.-Y. Zhang, F. Campi, L. Lötgering, A. F. Koenderink, and P. M. Kraus, Extreme-ultraviolet shaping and imaging by high-harmonic generation from nanostructured silica, *Phys. Rev. Lett.* **128**, 223902 (2022).